HHS Public Access

Author manuscript

Neuroimage. Author manuscript; available in PMC 2020 March 01.

Published in final edited form as:

Neuroimage. 2019 March ; 188: 616–627. doi:10.1016/j.neuroimage.2018.12.039.

Modeling Glymphatic System of the Brain Using MRI

Esmaeil Davoodi-Bojd[1,2], **Guangliang Ding**[1], **Li Zhang**[1], **Qingjiang Li**[1], **Lian Li**[1], **Michael Chopp**[1,3], **ZhengGang Zhang**[1], and **Quan Jiang**[1,3]

[1]Department of Neurology, Henry Ford Health System, Detroit, MI, USA

[2]Department of Radiology, Henry Ford Health System, Detroit, MI, USA

[3]Department of Physics, Oakland University, Rochester, MI, USA

Abstract

The glymphatic system is functional waste clearance path from the brain parenchyma through dynamic exchange of cerebrospinal fluid (CSF) with interstitial fluid (ISF). Impairment of glymphatic waste clearance is involved in the development of neurodegenerative conditions. Despite many recent studies investigating the glymphatic system, few studies have tried to use a mathematical model to describe this system, quantitatively. In this study, we aim to model the glymphatic system from the kinetics of Gd-DTPA tracer measured using MRI in order to: 1) map the glymphatic system path, 2) derive kinetic parameters of the glymphatic system, and 3) provide quantitative maps of the structure and function of this system. In the proposed model, the brain is clustered to similar regions with respect to the profile of contrast agent (CA) density measured by MRI. Then, each region is described as a two-compartment kinetic model ‘derived from’ or ‘clears to’ its neighbors with local input function. We thus fit our model to the local cerebral regions rather than to the averaged time signal curve (TSC) of the whole brain. The estimated parameters showed distinctive differences between diabetes mellitus (DM) and control rats. The results suggest that in a typical DM brain the CSF bulk speed in the para-vasculature network is low. In addition, the resulting maps indicate that there may be increased binding and decreased absorbing of large molecules in a diabetic compared with a non-diabetic brain. The important contribution of this work was to fit the model to the local regions rather than to the averaged time signal curve (TSC) of the whole brain. This enabled us to derive quantitative maps of the glymphatic system from MRI.

Keywords

Glymphatic system; contrast enhanced MRI; diabetes mellitus; multi-compartment kinetic modeling

Correspondence to: Quan Jiang.

1. Introduction

Recent studies (Iliff *et al.*, 2012; Iliff *et al.*, 2013b; Rangroo Thrane *et al.*, 2013; Xie *et al.*, 2013; Plog *et al.*, 2015; Louveau *et al.*, 2017) have fundamentally transformed the traditional model of cerebrospinal fluid (CSF) hydrodynamics. Traditionally, it is believed that CSF produced by the choroid plexus located in all 4 ventricles flows into the subarachnoid space surrounding the brain and from here exits the cranial cavity by outflow along cranial and spinal nerves and the arachnoid villi. However, new imaging measurements have shown that CSF also can be recycled back into the brain and exchanged with interstitial fluid (ISF) (Iliff *et al.*, 2012; Iliff *et al.*, 2013b; Rangroo Thrane *et al.*, 2013; Xie *et al.*, 2013; Plog *et al.*, 2015). The functional waste clearance path from the brain parenchyma through dynamic exchange of CSF with ISF is identified as the glymphatic system. The glymphatic system provides a pathway of convective fluid flow that drives clearance of interstitial solute from the brain parenchyma. A large proportion of subarachnoid CSF enters the interstitium through para-arterial pathways and exchanges with ISF (a process referred to herein as CSF-ISF exchange), and both are cleared together with any associated solutes along specific para-venous pathways (Iliff *et al.*, 2012; Iliff *et al.*, 2013a). The glymphatic system is primarily active during natural sleep (Jessen *et al.*, 2015). Impairment of the glymphatic clearance is involved in the development of neurodegenerative conditions, including diabetes, Alzheimer`s disease, traumatic brain injury (TBI), stroke and glaucoma (Iliff *et al.*, 2012; Xie *et al.*, 2013; Gaberel *et al.*, 2014; Kyrtsos and Baras, 2015; Plog *et al.*, 2015; Wostyn *et al.*, 2015; Ramirez *et al.*, 2016; Venkat *et al.*, 2016; Jiang *et al.*, 2017).

Studies of the glymphatic system have shown that several factors can alter the waste clearance performance of the glymphatic system, e.g., vessel stiffness and heart rate (Kyrtsos and Baras, 2015), body posture (Lee *et al.*, 2015), ventricular size (Jessen *et al.*, 2015). In addition, brain diseases, especially neuro-degenerative diseases may evoke impairment of glymphatic system. However, few studies have attempted to model the flow through the glymphatic pathways in order to derive quantitative parameters from MRI data. Having such a model may yield improved: 1) understating the glymphatic system dynamics, 2) diagnosis, monitoring, and prognosis of the disease, 3) therapeutic approached.

For quantitative modeling of the glymphatic system using MRI, first, the map of glymphatic path needs to be identified. Then, the dynamics of the fluid (CSF-ISF) flowing through these pathways should be modeled using appropriate equations. Finally, an optimization method should be employed to estimate the model's parameters from MRI measurements. Therefore, a dynamic MRI paradigm using a contrast agent tracer (such as GD-DTPA) should be used so that the 'signal change' inside the glymphatic pathways can be measurable.

Despite many recent studies that investigated the glymphatic system, few studies have employed a mathematical model to describe this system quantitatively. In (Ratner *et al.*, 2015; Ratner *et al.*, 2017), optimal mass transport (OMT) was used to model the glymphatic flow vector field from MRI data and to map the glymphatic pathways. This method shows promising results in identifying the glymphatic channels; however, it does not provide quantitative measures for the dynamics of the glymphatic system. Moreover, it cannot

identify efflux path which is important in investigating the glymphatic system. Kinetic analysis was also incorporated to model the transport patterns of Gd-DTPA inside the rat's brain at three different postures (Lee *et al.*, 2015). In this work, the brain was divided into two parts, injection site and all other brain tissues. Then, the signal changes of tracer concentration (measured from MRI) of these two regions were used to derive the kinetic parameters of the brain, employing a two-compartment kinetic model. The limitation of this method is that the model parameters are calculated using global input function from the injection site, therefore, it does not provide accurate measures for local regions, separately, due to the difficulty in determining the input function corresponding to each region.

In the current study, we aim to model the glymphatic system from the kinetics of GD-DTPA tracer in order to: 1) map the glymphatic system pathways, 2) derive kinetic parameters of the glymphatic system, and 3) provide quantitative maps of the structure and function of this system. Diabetes mellitus (DM) is a major health problem with an estimated incidence of nearly 25.8 million people (8.3% of the US population) (CDC&P, 2011). A common factor among all diabetes related pathologies is their association with both micro- and macro-vascular changes that develop throughout the progression of the disease, and that irreparable damage often occurs before symptoms of the disease are recognizable. The duration and severity of DM are also associated with changes in cerebrovascular structure, suggesting that the effects are cumulative (Saczynski *et al.*, 2009). Using MRI, we previously investigated the impairment of the glymphatic system in diabetes animals and demonstrated that the brain solute clearance is reduced in diabetes by monitoring the clearance profile of the injected GD-DTPA contrast agent tracer (Jiang *et al.*, 2017). Thus, we used the MRI data of healthy and DM animals to assess the performance of our model in differentiating affected tissues.

2. Methods

All experimental procedures were conducted and performed in accordance with guidelines of National Institute of Health (NIH) for animal research under a protocol approved by the Institutional Animal Care and Use Committee of Henry Ford Hospital, and experimental guidelines of ARRIVE (items 8, 10 to 13). All experimental procedures were approved by the Institutional Animal Care Committee of Henry Ford Hospital.

Ten rats (5 healthy controls and 5 diabetics) were evaluated using a Contrast-Enhanced Magnetic Resonance Imaging (CE-MRI) protocol using Gd-DTPA contrast agent as described in our previous publications (Jiang *et al.*, 2017). MRI measurements were performed with a 7T system (Bruker-Biospin, Billerica, MA, US). A birdcage type coil was used as the transmitter and a quardrature half-volume coil as the receiver. During MRI measurements, breathing of animals was monitored (Biopac Systems Inc., Goleta, CA, USA) and anesthesia was maintained using a gas mixture of N2O (70%) and O2 (30%) with 1.0–1.5% isoflurane (Piramal Inc., Bethiehem, PA, US). Stereotactic ear bars were used to minimize head movement during the MRI scan for all rats, and rectal temperature of animals was maintained at 37±1.0°C using a feedback controlled air heating blower (Rapid Electric, Brewster, NY, US). T1-weighted images were acquired using a 7Tesla animal scanner with TR/TE=15/4ms and acquisition voxel size of 0.125×0.167×0.167 mm^3 and reconstructed to 0.125×0.125×0.17 mm^3. A total of 80 μl of the paramagnetic contrast agent was delivered

intrathecally at an infusion rate of 1.6 μl per minute (total infusion time 50 min) by using a 100μL syringe (Hamilton Robotics, Reno, NV, US) with an infusion pump (Harvard Apparatus, Holliston, MA, US). Up to 62 3D-T1-weighted volumes (in approximately every 5 minutes) were acquired until 6 hours after intra-cisterna magna (ICM) contrast agent delivery.

This enables us to monitor the propagation profile of the tracer in the brain during the experiments. For each voxel, x, the intensity value at each time, $I_x(t)$, is used to derive **time signal curve (TSC)** (Lee *et al.*, 2015), representing the time profile of the tracer's density.

$$TSC_x(t) = \frac{I_x(t) - I_x(t_0)}{I_x(t_0)} \quad (1)$$

in which t_0 is any time before injection.

2.1. Preprocessing

Motion Correction and Brain Extraction—The animal's brain can move drastically during our long (~6 hours) imaging experiments. Moreover, the T1 weighted images in this work include all non-brain tissues of the animal`s head, as shown in Fig. 1, which need to be masked in order to reduce the computational complexity of the subsequent processes. In addition, the deformation of the non-brain tissues during the experiment affects proper co-registration of the volumes.

For each animal, we compensated for the head motion in two steps, before and after brain extraction to correct severe head motions and small brain motions, respectively. To assess the head motion, visually, we derived standard deviation (STD) map from the images. The value of each voxel in this map equals to the standard deviation of the values of this voxel in the T1-weighted volumes during the experiment, see Fig. 1. We chose the STD map because it can determine how much the brain has moved during the experiments by highlighting the boundaries.

In the first step, the whole head is corrected for motion using coarse co-registration algorithm (Friston *et al.*, 2007). Then, we drew manually a mask on the STD map (as shown in Fig. 1, bottom row) so that the resulting mask should encompass the entire brain volume. Then, for each volume, the mask is refined to the brain boundaries using morphological operations in MATLAB. Next, the brain extracted volumes were compensated for the head motion, again.

For the motion correction steps, all the volumes were co-registered to the first time point volume using a coarse registration algorithm in SPM8 toolbox with normalized mutual information (NMI) cost function with trilinear interpolation (Friston *et al.*, 2007). Also, we set the window size of spatial Gaussian smoothing to 4 mm. The average distance between sample points in the optimization iterations were chosen as 4, 2, and 1 mm in the first step, and as 4, 2, 1, 0.5, 0.25 mm in the second step of the motion correction.

In Fig. 1, the resulting images of motion correction steps are shown for a typical case. Four time points, 0, 100, 200, and 300 minutes after injection are displayed, representing the accumulation and dissipation of the tracer during the experiment. Although the motion cannot be seen clearly using these images, the corresponding STD maps can show the level of brain motion. As it can be seen from the STD maps, the edges have become clearer after the motion correction steps.

Common Spatial Space—Moreover, to have the same spatial space for all animals, we selected one animal as the reference and aligned all the other animal's images to it. To this end, we aligned the AVG maps (calculated by averaging all co-registered and brain extracted T1-weighted images) of each animal to the reference animal using an affine registration algorithm in SPM8 and used the resulting transformation function to move all the T1-weighted volumes to the *common space*. Please note that we calculated the TSCs (equation (1)) *in the common space* for all animals.

2.2. Down-sampling and Clustering

To reduce the computational complexity, first, we down sampled all the volumes from 256*256*96 to 128*128*48 images which resulted in the voxel size of 0.25*0.25*0.34 mm^3. Then, we clustered the voxels of each brain into similar regions based on the propagation profile of the tracer during the experiment. This would also reduce the computations as well as reduce the effect of noise and uncorrected head motions.

For the similarity criterion used in the clustering, we chose the derivative of the TSCs instead of the actual signal curves in order to cluster the voxels based on the dynamics of tracers only. As an example, the plots of the TSCs and their derivatives of a typical case are shown in Fig. 2.

A hierarchical clustering scheme that employs a k-means clustering algorithm was used. In this scheme, first, the k-means clustering algorithm splits the whole voxels into two clusters. Then, it sequentially splits each of the resulting clusters into two new sub-clusters, if 1) the number of voxels of the cluster is bigger than 100, and 2) the *within cluster inconsistency* (WCI) is greater than 0.125. WCI for a cluster, c_j, of N_j voxels, in which a voxel i has the derivative signal $d_j(i,n)$, $n=1,\ldots,T$, is defined as

$$WCI_j = \frac{\max_{n=1,\ldots,T} std\left(d_j(i,n), i=1,\ldots,N_j\right)}{\max_{n=1,\ldots,T} std(d(i,n), i=1,\ldots,N)} \quad (2)$$

in which T is the number of time points.

This procedure continue until there is no cluster that can be split anymore. Here, the k-means clustering algorithm is based on the Euclidian distance between the absolute value of derivative signals of the voxels. After the clustering, the average TSCs of the voxels inside each cluster is assigned to that cluster.

2.3. Scalar Maps

Having the time signal curves (TSC) for each cluster, we calculated three parameters that can help to understand the response of the glymphatic system to Gd-DTPA injection.

1. The arrival time, t_a, which is defined as the time that the tracer arrives to each cluster region after the injection,
2. the infusion flow rate, (IR), defined as the slope of TSC of each cluster between arrival time, t_a, and the time that TSC goes to its maximum value, t_{max}, and
3. the tracer residual, (Res), which is defined as the amount of Gd-DTPA tracer that remains in the tissues at the end of experiment.

We estimated the arrival time, t_a, for each cluster from its time signal curve by finding the time point that the signal rises and keeps rising for at least three successive time points. The infusion flow rate was estimated using the following equation,

$$IR = \frac{TSC(t_{max}) - TSC(t_a)}{t_{max} - t_a}, \quad (3)$$

and the tracer residual was calculated by

$$Res\% = \frac{TSC(t_{end}) - TSC(t_a)}{TSC(t_{max})} \times 100, \quad (4)$$

in which TSC(t_a) is actually equal to zero.

2.4. Kinetic Modeling

As suggested by (Lee *et al.*, 2015) we used a two-compartment structure shown in Fig. 3 to model the GD-DTPA Changes in the glymphatic system. The differential equations describing this model are

$$\frac{dC_1(t)}{dt} = K_1 C_p(t) - (k_2 + k_3)C_1(t) + k_4 C_2(t) \quad (5)$$

$$\frac{dC_2(t)}{dt} = k_3 C_1(t) - k_4 C_2(t) \quad (6)$$

which, C_p is the tracer concentration in the para-artery where the tracer diffuses to its adjacent tissues, C_1 is the concentration of free tracers inside the tissue, and C_2 is the concentration of bounded tracers. In the glymphatic system, the tracer concentration in the para-vascular spaces can be used to estimate C_p. K_1 determines the scaling factor for the

concentration, k_2 is the washout coefficient, and k_2 and k_3 are the binding coefficients between compartments 1 and 2.

Using Laplace transform, the solution for the differential equations (5) and (6) is

$$C(t) = C_1(t) + C_2(t) = \frac{K_1}{2}\left[(1+A)e^{-(B+M)t} + (1-A)e^{-(B-M)t}\right] * C_p(t) \quad (7)$$

in which * represents mathematical convolution and

$$M = \frac{1}{2}\sqrt{(k_2+k_3+k_4)^2 - 4k_2k_4} \quad (8)$$

$$A = \frac{k_2 - k_3 - k_4}{2M} \quad (9)$$

$$B = \frac{k_2 + k_3 + k_4}{2}. \quad (10)$$

Model Fitting—The model described in equation (7) has 4 unknown parameters K_1, k_2, k_3 and k_4 which need to be estimated from the TSCs measured from the regions (clusters). In the model fitting process, the corresponding TSC of each region can be assumed as $C(t)$, since it represents the concentration of all CA molecules in that region. However, estimating the plasma concentration or the CA concentration in the para-arteries is challenging because identifying the arteries from the images is difficult. In (Lee *et al.*, 2015) the authors adopt a two compartment vascular permeability model and identified the subarachnoid cisterna magna (CM) space as the injection site for input function (IF) to estimate the glymphatic kinetic parameters of the whole brain. However, one of the leading sources of error in quantifying perfusion and permeability is the determination of the arterial input function (AIF) which becomes even more severe in the modeling of glymphatic system since the errors from IF delay and dispersion in the glymphatic system are much larger than in the vascular system. The AIF is determined by its location relative to the tissue concentration curve, and can either be classified as a global or regional AIF. The most common method uses a global AIF, typically located in the middle branch of the middle cerebral artery (MCA), which implies that a single AIF measurement is used voxel-wise over the entire brain. Consequently, AIF delay and dispersion may occur and has been shown to introduce substantial errors in cerebral blood flow (CBF), mean transit time (MTT), and permeability (Wu *et al.*, 2003; Calamante *et al.*, 2006; Ferreira *et al.*, 2010; Calamante, 2013; Nejad-Davarani *et al.*, 2017a, b).

In this work, benefiting from clustering the tissues based on the dynamic response of the tissues to the CA infusion, we defined an approach to find the local input function for each region which could provide a big advantage over the traditional global IF approach (Lee *et al.*, 2015) to reduce errors in the modeling of glymphatic system. To this end, first, for each region (cluster), R_j, the neighboring regions, R_{jk}, k=1,…,N_j were found based on their shared boundaries. Then, three criteria were defined to find the cluster that drives that region (R_j) dominantly among those N_j neighbors,

$$\max_{k \in \{1,\ldots,N_j\}} t_{0jk} \mid \begin{cases} t_{0jk} \leq t_{0j} \\ r_{ajk} \geq r_{aj} \\ t_{mjk} \leq t_{mj} \end{cases} \quad (11)$$

These criteria are based on the arrival times, t_a, the early infusion rates (defined as the slope of TSC early after t_a), r_a, and the time of maximum of the TSCs, t_m.

Now, the TSC of the neighboring cluster (Rjk^*) found from equation (11) is considered as the local input function $C_p(t)$ for cluster j. In other words, the kinetic model for cluster j is written as:

$$TSC_j(t) = \frac{K_1}{2}\left[(1+A)e^{-(B+M)t} + (1-A)e^{-(B-M)t}\right] * TSC_{jk*}(t) \quad (12)$$

with four unknown parameters.

Employing non-linear least square optimization tool in MATLAB (Release 2012b, The MathWorks, Inc., Natick, Massachusetts, United States), we estimated the unknown parameters for each cluster.

As suggested by (Lee *et al.*, 2015), two quantities can be defined based on the estimated parameters of equation (12), *retention* and *loss* which are defined as,

$$retention = \frac{k_3}{k_4} \quad (13)$$

$$loss = \frac{k_2}{1 + \frac{k_3}{k_4}} \quad (14)$$

'Retention' is assumed to characterize the fraction of the tracers that remain bonded with large molecules and thus can reduce the CSF movement speed. Thus, higher values of retention can demonstrate slower clearance of waste particles though the CSF. In addition,

'*loss*' measures the portion of particles that continue to flow through the glymphatic system by going back to the para-veins.

A simple way to characterize the glymphatic system is to estimate the clearance signature of the injected CA by fitting a *one exponential model* to the relaxing phase of the TSCs. The relaxing phase of a TSC starts from the time that the signal reached to its maximum and ends at the end of experiment. It was assumed that the contrast agent particles are clearing out from the glymphatic system during this time. Therefore, estimating the time constant from the relaxing phase of TSC may identify how well the glymphatic system clears the wastes. We estimated this parameter, τ, from the following one exponential model,

$$TSC_{relax}(t) = TSC(t_m) \cdot e^{-\frac{t - t_m}{\tau}}, t_m \leq t \quad (15)$$

2.5. Data and Code Availability

The MRI data used in this study may be shared on request from the corresponding author, Q. J. The data are not publicly available due to our ongoing research projects. The in house MATLAB codes used in this study are available on request from the corresponding author, Q. J.

3. Results

In this section, first we evaluate our proposed approach using artificial data. Then we apply the methods to model real data.

3.1. Simulation

To generate artificial data for evaluating the methods proposed in this work, we solved the equations (5) and (6) using finite difference method, numerically. To this end, first we generated an imaginary path for contrast agent distribution consisting of three parts as shown in Fig. 4A. Region 1 is assumed to be the para-vascular path. Regions 2 and 3 correspond to brain tissues with different kinetic specifications. We assumed one injection site (IS) to infuse the contrast agent to the brain and four drain holes (DH) to clear it from the brain, as shown in Fig. 4A. The imaginary contrast agent (CA) is assumed to infuse to the brain with a constant rate of 100 for 60 minutes. Then, the following differential equations were solved numerically to generate the artificial data.

$$C_1(x, t + dt) = C_1(x, t) + dt \cdot \left(K_1^x C_p(x, t) - \left(k_2^x + k_3^x\right) C_1(x, t) + k_4^x C_2(x, t)\right) \quad (16)$$

$$C_2(x, t + dt) = C_2(x, t) + dt \cdot \left(k_3^x C_1(x, t) - k_4^x C_2(x, t)\right) \quad (17)$$

$$C_p(x,t) = \sum_{y \in N_x} C_1(y,t) \quad (18)$$

Here, x represents the current voxel and its neighboring voxels are $y \in N_x$. We assumed N-8 adjacency for the neighbors. Time step, dt, was set to 0.01 minutes and in each step, equations (16) and (17) were updated, successively, until 360 minutes. We set the kinetic parameters for region 1 as $K_1=k_2=400$, $k_3=4$, and $k_4=3.9$ min^{-1}, region 2 as $K_1=k_2=100$, $k_3=4$, and $k_4=2$ min^{-1}, and region 3 as $K_1=k_2=80$, $k_3=4$, and $k_4=0.8$ min^{-1}.

The resulting temporal profiles for $C(t)=C_1(t)+C_2(t)$ are shown in Fig. 4 B,C, and D, for the regions 1, 2, and 3, respectively.

To have a ground truth data for the parameters, we estimated the parameters directly from the clean data without using the clustering method described in section 2.2. The ground truth maps for the parameters of t_a, t_{max}, residual, and infusion rate are shown in Fig. 4 E, F, G, and H, respectively. It can be seen clearly how the imaginary contrast agent infuses through the different regions. It reaches to the voxels close to the infusion site (IS) sooner and clears out faster.

Next, to investigate the effect of noise on the methods used in this work, we added white Gaussian noise to the data with different signal to noise ratios (SNR) of 500, 200, 100, 80, 50, and 30. The standard deviation of the Gaussian noise for each SNR value was calculated as m/SNR in which m is the average of the image intensities without any noise. In each experiment, we compared the resulting parameters, t_a, t_{max}, infusion rate, residual, τ, loss, and retention, from the models with the ground truth parameters by calculating the mean absolute percentage error (MAPE),

$$MAPE = \frac{1}{N}\sum_{i=1}^{N} \frac{\left|P_i - \hat{P}_l\right|}{\hat{P}_l} \times 100 \quad (19)$$

in which P_i is the estimated parameter in voxel i, $\hat{P}_l$ is the corresponding ground truth value, and N is the number of voxels. In Fig. 5, the MAPE values for different parameters on different regions in different SNRs are shown.

In section 2.2 we stated that for the similarity criterion used in the clustering, we used the derivative of the TSCs instead of the actual signal curves in order to cluster the voxels based on the dynamics of tracers only. Here, we investigated the effect of using the derivative of the signal instead of the actual signal. The blue and red bins correspond to the MAPEs from using the actual TSCs and the derivative of the TSCs for the clustering, respectively. It can be seen from the Fig. 5 that the parameters are estimated with less errors if the derivative of the TSCs is used for the clustering. However, as the SNR goes down, the two methods show comparable errors.

Moreover, it can be seen that arrival time, t_a, is the most robust parameter to the noise and the infusion rate is the worst one. By comparing the MAPE of the estimated parameters in the three regions (see Fig 4.A), it can be seen that the estimated parameters have more errors in region 2 than the other two regions. As an example, the MAPE map of residual parameter for the SNR of 80 is shown in Fig. 5H. Here there is higher errors for the estimated parameters in the regions far from the infusion site. This is mainly due to the attenuation of the TSCs in these regions.

3.2. Real Data

We applied the aforementioned steps described in section 2 to process the MRIs of 5 healthy control and 5 DM animals and to fit the kinetic model proposed in section 2.4. In order to evaluate our proposed model, we also applied the kinetic model used in (Lee *et al.*, 2015).

Our clustering algorithm described in section 2.2 resulted in 400 to 550 clusters for the 10 individual data sets. The difference in the number of final clusters is caused by the difference between the brains and between the experiments. The number of clusters was not considered to affect fitting the model as long as it is 1) large enough so that small tissues that have distinctive different TSCs from their neighbors are not absorbed into other clusters, and 2) small enough to avoid high computational time.

The clustering maps for two typical cases (One healthy control and one DM animal) are shown in Fig. 6A and B in which different clusters are shown with different colors. Since each color represented a region with similar profile of CA concentration, a rough view of the path of the Gd-DTPA tracer may be seen on these images. The paths are supposed to be realized by connecting ‘vessel’ shaped clusters. Moreover, deep tissues where the tracer did not reach to had been aggregated in bigger clusters, as we expected. The corresponding scalar maps for these cases are shown in Fig. 6C, D, E, F, G, and H as well.

By comparing the arrival time (t_a) maps shown in Fig. 6C and D, it can be seen that the tracer took longer to reach to the anterior-frontal para-vascular spaces in the DM animal; suggesting lower *bulk* speed of CSF in the para-vasculatures. However, based on Fig. 6E and F, the infusion rate patterns appeared similar for animals in both groups but with higher rate in the inferior paravascular path of the DM animal. These two findings seem to be contradictory, however, this can be caused by higher para-vascular spaces in the DM animal (Jiang *et al.*, 2017), so that although the infusion rate is high, the tracer particles need more time to fill out the space and move forward to the next location.

Fig. 6G and H also show that much higher amount of the tracer remains in the DM brain. These data are in agreement with our previous findings (Jiang *et al.*, 2017) that reported the waste clearance system of the brain is reduced in DM brain.

We fitted the model proposed in section 2.4 to each animal’s data i.e., the TSCs of the clusters. In Fig. 7 the resulting estimated parameters of the two models (one-exponential and two-compartment kinetic models with local input function) for one typical healthy control and one typical DM animal are shown for visual comparison which demonstrates the differences of the maps for the two animals.

To have a quantitative comparison between our proposed model, one-exponential model, and two-compartment kinetic model used by (Lee *et al.*, 2015), the boxplots of their estimated parameters from five healthy and five DM animals are shown in Fig. 8. For each parameter, a two sample t-test with the hypothesis that if the mean values of that parameter for the two groups are equal was performed and the resulting p-value is displayed on each plot.

It can be seen that in the DM animals: 1) the clearance time constant, τ, calculated from one-exponential model is increased (p-value=0.012), 2) the *retention* and *loss* parameters estimated from the two-compartment kinetic model used by (Lee *et al.*, 2015) with global IF are increased (p-value=0.151) and decreased (p-value=0.027), respectively, and 3) the *retention* and *loss* parameters estimated from our proposed the two-compartment kinetic model are increased (p-value=0.031) and decreased (p-value=0.005), respectively, compared with healthy control animals.

These data are consistent with previous findings that suggest the waste clearance is slower in diabetic brain (Jiang *et al.*, 2017). The higher values of *retention* parameter in many regions in diabetic brain, (Fig. 7C and D), may suggest that more numbers of large molecules remain bound in a diabetic brain. In addition, lower values of *loss* parameter, especially in deep tissues of the diabetic brain, may suggest that reduced numbers of large molecules circulate back to (are absorbed by) the glymphatic system in the DM brain (Fig. 7E and F).

The high retention values seen in the top central region of the control brain (Fig. 7C) may be caused by low concentration of CA. As suggested by Fig. 6C, small amounts of CA reached to the top central region which is mainly due to the quick clearance of CA from the regions around the para-vasculature in the control rats. Low CA concentration could also extend the clearance time in this region (as seen in Fig. 8A).

Compared with the method used by (Lee *et al.*, 2015), our proposed method evidently differentiates the glymphatic system of the healthy and diseased animals. This has been mainly achieved by the capability of our proposed approach to modeling the local CA dynamics from the target and neighboring regions. Moreover, another important superiority of the proposed method is that it provides quantitative maps which can be used to unveil the characteristics of glymphatic system in different parts of brain.

4. Discussion

In this work, by modeling the dynamic of the tracer movement through the glymphatic path, we developed an approach to quantitatively model the glymphatic system. Using a CE-MRI protocol with Gd-DTPA contrast agent, the time signal curves (TSCs) representing the CA density in each region were analyzed using cluster analysis.

We propose an approach to fit a two-compartment kinetic model with local input function to the TSCs of the clusters in order to derive quantitative maps representing the dynamics of the glymphatic system. Compared to previous models (one-exponential and two-compartment kinetic model with global input function), the proposed model generates more distinctive measures between two groups of healthy and DM animals. The resulting maps show increased binding and decreased loss of tracers in a diabetic brain.

One of the important contributions of this work was to fit the model using the local input function rather than global input function and thereby to reduce errors. For long time, it was a major challenge to reduce the leading sources of error induced by arterial input function (AIF) in quantifying cerebral perfusion and permeability. Due to its convenience, current cerebral perfusion and permeability analysis is still dominated by global AIF. Global AIF may produce two major errors resulting from AIF delay and dispersion. Delay is defined as the delay in arrival time between the AIF and tissue concentration curve, whereas dispersion is the consequence of the contrast bolus becoming dispersed over time. Although the major error from global AIF in the cerebral perfusion and permeability analysis has been recognized for more than decade, it has not been fully resolved. Here, we have shown promising results when applying a novel model of the brain vascular system based on laws of fluid dynamics and vascular morphology to address the dispersion and delay of the AIF and to estimate the local AIF in perfusion and permeability analysis (Nejad-Davarani *et al.*, 2017a, b). The global IF delay and dispersion for the glymphatic system are much larger and could cause more error than that for the vascular system. In the current study, we tested a new cluster analysis approach to obtain the local IF. By direct comparison with the global IF model, our local IF modeling data exhibited tighter data distribution with higher statistical significance between DM and control groups (Fig. 8). Our results demonstrate that the glymphatic model with local IF may be a useful tool for obtaining more accurate estimation of parameters in glymphatic system studies.

Another advantage of the proposed method is that it provides quantitative maps of the dynamics of the CA distribution into the brain's para-vascular system. These maps can be used to compare the characteristics of glymphatic system in different regions of brain. Moreover, our quantitative maps of glymphatic system may be used for optimizing experimental parameters such as CA dose, imaging intervals, imaging duration, etc. For example, many regions will receive little amount of CA if insufficient doses of CA is applied. This can make the experiment worthless, especially if the interested region for investigation is within these areas. The imaging duration can be adjusted based on the residual and relaxation time constant, and it should be long enough so that the CA has started clearing out from the interested regions.

Several factors could affect modeling of glymphatic system, especially the relative large volume injection of contrast agent. The large injection volume may increase the intracranial pressure (ICP) and disturb the regular CSF flow, which may affect glymphatic influx and efflux patterns, and lead to pathophysiological complications and erroneous information. Previous studies demonstrated that an increase in ICP of about 2.5mmHg, a 50% increase from the baseline of 5.0mmHg, was observed with a rate of 2.0μL/min infusion in mice, although it did not cause reflux of subarachnoid CSF back into the ventricular CSF compartments, which suggested that the physiological direction of CSF bulk flow is maintained (Kress *et al.*, 2014). In rat, ICP was slightly increased, approximately 6.3% from baseline of 4.8mmHg to 5.1mmHg with the infusion rate of 3.0μL/min, and no ICP changes were observed with an infusion rate of 0.34μL/min (Bedussi *et al.*, 2017). We have performed MRI studies to investigate the response of the glymphatic system to the rate of infusion of Gd-DTPA (Ding *et al.*, 2018). We found that infusion rate of 2.92μL/min induced an evident accumulation of tracer in the fourth ventricle near the cisterna magna and the rate

1.6μL/min does not cause this kind of tracer accumulation (Ding *et al.*, 2018). All of current MRI investigations of glymphatic system employed relatively large volume contrast agent due to the relatively low sensitivity of MRI compared with two photo imaging (Iliff *et al.*, 2013a; Lee *et al.*, 2015; Ratner *et al.*, 2017; Lee *et al.*, 2018). However, MRI has great potential for translating its markers into clinic over two-photon laser scanning microcopy which is invasive and not suitable for whole brain study, especially deep brain tissues.

CSF-ISF impairment after diabetes may be associated with numerous complications including vascular dysfunction, loss of paravascular aquaporin-4 (AQP4) immunoreactivity, oxidative stress, neurotoxicity, defects in neural insulin and amyloid metabolism, etc (Qiu *et al.*, 2014; Jiang *et al.*, 2017). A common factor among all of these diabetes related pathologies is their association with both micro-and macro-vascular changes that develop throughout the progression of the disease and that irreparable damage often occurs before symptoms of the disease are recognizable (Qiu *et al.*, 2014; Mayeda *et al.*, 2015). Our study of the same animal model of diabetes showed the presence of patched micro-thrombosis and BBB leakages assayed by vascular and parenchymal fibrin deposition mainly in the hippocampus of diabetic rats (Jiang *et al.*, 2017). Moreover, double immunofluorescent staining shows the presence of diffuse activated-astrocytes in areas with micro-thrombosis and BBB leakage in the hippocampus of DM rats, which was accompanied with substantial loss of paravascular AQP4 immunoreactivity (Jiang *et al.*, 2017). Our results are consistent with published studies by others showing that astroglial AQP4 water channel is expressed in a highly polarized manner in paravascular astrocytic end-feet and micro-ischemia induces AQP4 de-polarization (Nielsen *et al.*, 1997; Amiry-Moghaddam *et al.*, 2004; Alvestad *et al.*, 2013). Previous studies has demonstrated that AQP4 plays important role on glymphatic system (Iliff *et al.*, 2012; Kress *et al.*, 2014; Benveniste *et al.*, 2018). An important neuropathological mechanism in the diabetic brain is the accumulation of misaggregated proteins, including senile plaques comprised of amyloid-β (Aβ) (Szeman *et al.*, 2012; Prasad *et al.*, 2014). Previous studies have demonstrated that the glymphatic system regulates the clearance of Aβ (Iliff *et al.*, 2012). Patients with T2DM who developed AD exhibited extensive accumulation of Aβ and neuritic plaques (Janson *et al.*, 2004). Experimental studies show that diabetes induced by high-fat and/or sugar diet (HFD) leads to Aβ accumulation in the brain (Ho *et al.*, 2004; Cao *et al.*, 2007; Yang *et al.*, 2013; Mehla *et al.*, 2014). Recent epidemiological studies indicate that diabetes significantly increases the risk of developing Alzheimer Disease (AD), suggesting that diabetes may play a causative role in the development of AD pathogenesis (Baglietto-Vargas *et al.*, 2016). It is likely that the impairment of the glymphatic system and associated accumulation of molecular waste in the paravascular space activate a cascade of inflammatory responses that lead to neurovascular disruption, including the increase of the paravascular space, a pathological feature in DM brain (Wuerfel *et al.*, 2008). In this work, using kinetic modeling of contrast agent distribution through the paravascular spaces, for the first time, we introduce five different quantitative maps for the glymphatic system which can reveal an overall view of the circulation paths of the glymphatic system, as shown in Fig. 6 and Fig. 7. The accumulation of the CA in the diabetic brains in these maps is a non-invasive evidence of the waste accumulation in diabetes. A similar methodology may be employed for investigation of other brain diseases.

In this work, we clustered the voxels into large regions in order to increase signal to noise as well as to decrease the computational complexity. This may cause loss of small paths or small regions from analysis if they are incorporated into their big neighboring clusters. Deriving detailed maps that can show the narrow paths of the glymphatic system may require additional complex complicated models along with a well-planned experiment with optimized dose and imaging parameters.

Acknowledgments

Funding

This work was financially supported by NIH R21 AG052735, RO1 NS097747, and RF1 AG057494.

Abbreviations

DM	diabetes mellitus
CA	contrast agent
TSC	time signal curve
IF	input function

6. References

Alvestad S, Hammer J, Hoddevik EH, Skare O, Sonnewald U, Amiry-Moghaddam M, et al. Mislocalization of AQP4 precedes chronic seizures in the kainate model of temporal lobe epilepsy. Epilepsy Res 2013; 105(1–2): 30–41. [PubMed: 23357720]

Amiry-Moghaddam M, Xue R, Haug FM, Neely JD, Bhardwaj A, Agre P, et al. Alpha-syntrophin deletion removes the perivascular but not endothelial pool of aquaporin-4 at the blood-brain barrier and delays the development of brain edema in an experimental model of acute hyponatremia. FASEB journal : official publication of the Federation of American Societies for Experimental Biology 2004; 18(3): 542–4. [PubMed: 14734638]

Baglietto-Vargas D, Shi J, Yaeger DM, Ager R, LaFerla FM. Diabetes and Alzheimer's disease crosstalk. Neuroscience and biobehavioral reviews 2016; 64: 272–87. [PubMed: 26969101]

Bedussi B, Naessens DMP, de Vos J, Olde Engberink R, Wilhelmus MMM, Richard E, et al. Enhanced interstitial fluid drainage in the hippocampus of spontaneously hypertensive rats. Scientific reports 2017; 7(1): 744. [PubMed: 28389645]

Benveniste H, Liu X, Koundal S, Sanggaard S, Lee H, Wardlaw J. The Glymphatic System and Waste Clearance with Brain Aging: A Review. Gerontology 2018: 1–14.

Calamante F Arterial input function in perfusion MRI: a comprehensive review. Progress in nuclear magnetic resonance spectroscopy 2013; 74: 1–32. [PubMed: 24083460]

Calamante F, Willats L, Gadian DG, Connelly A. Bolus delay and dispersion in perfusion MRI: implications for tissue predictor models in stroke. Magnetic resonance in medicine : official journal of the Society of Magnetic Resonance in Medicine / Society of Magnetic Resonance in Medicine 2006; 55(5): 1180–5.

Cao D, Lu H, Lewis TL, Li L. Intake of sucrose-sweetened water induces insulin resistance and exacerbates memory deficits and amyloidosis in a transgenic mouse model of Alzheimer disease. The Journal of biological chemistry 2007; 282(50): 36275–82. [PubMed: 17942401]

CDC&P. National diabetes fact sheet: General information and national estimates on diabetes in the united states. 2011.

Ding G, Chopp M, Li L, Zhang L, Davoodi-Bojd E, Li Q, et al. MRI investigation of glymphatic responses to Gd-DTPA infusion rates. Journal of neuroscience research 2018; 96(12): 1876–86. [PubMed: 30272825]

Ferreira RM, Lev MH, Goldmakher GV, Kamalian S, Schaefer PW, Furie KL, et al. Arterial input function placement for accurate CT perfusion map construction in acute stroke. AJR Am J Roentgenol 2010; 194(5): 1330–6. [PubMed: 20410422]

Friston K, Ashburner J, Kiebel S, Nichols T, Penny W. Statistical Parametric Mapping - The Analysis of Functional Brain Images: Elsevier; 2007.

Gaberel T, Gakuba C, Goulay R, Martinez De Lizarrondo S, Hanouz JL, Emery E, et al. Impaired glymphatic perfusion after strokes revealed by contrast-enhanced MRI: a new target for fibrinolysis? Stroke; a journal of cerebral circulation 2014; 45(10): 3092–6.

Ho L, Qin W, Pompl PN, Xiang Z, Wang J, Zhao Z, et al. Diet-induced insulin resistance promotes amyloidosis in a transgenic mouse model of Alzheimer's disease. FASEB journal : official publication of the Federation of American Societies for Experimental Biology 2004; 18(7): 902–4. [PubMed: 15033922]

Iliff JJ, Lee H, Yu M, Feng T, Logan J, Nedergaard M, et al. Brain-wide pathway for waste clearance captured by contrast-enhanced MRI. The Journal of clinical investigation 2013a; 123(3): 1299–309. [PubMed: 23434588]

Iliff JJ, Wang M, Liao Y, Plogg BA, Peng W, Gundersen GA, et al. A paravascular pathway facilitates CSF flow through the brain parenchyma and the clearance of interstitial solutes, including amyloid beta. Science translational medicine 2012; 4(147): 147ra11.

Iliff JJ, Wang M, Zeppenfeld DM, Venkataraman A, Plog BA, Liao Y, et al. Cerebral arterial pulsation drives paravascular CSF-interstitial fluid exchange in the murine brain. The Journal of neuroscience : the official journal of the Society for Neuroscience 2013b; 33(46): 18190–9. [PubMed: 24227727]

Janson J, Laedtke T, Parisi JE, O'Brien P, Petersen RC, Butler PC. Increased risk of type 2 diabetes in Alzheimer disease. Diabetes 2004; 53(2): 474–81. [PubMed: 14747300]

Jessen NA, Munk AS, Lundgaard I, Nedergaard M. The Glymphatic System: A Beginner's Guide. Neurochem Res 2015; 40(12): 2583–99. [PubMed: 25947369]

Jiang Q, Zhang L, Ding G, Davoodi-Bojd E, Li Q, Li L, et al. Impairment of the glymphatic system after diabetes. J Cereb Blood Flow Metab 2017; 37(4): 1326–37. [PubMed: 27306755]

Kress BT, Iliff JJ, Xia M, Wang M, Wei HS, Zeppenfeld D, et al. Impairment of paravascular clearance pathways in the aging brain. Ann Neurol 2014; 76(6): 845–61. [PubMed: 25204284]

Kyrtsos CR, Baras JS. Modeling the Role of the Glymphatic Pathway and Cerebral Blood Vessel Properties in Alzheimer's Disease Pathogenesis. PloS one 2015; 10(10): e0139574. [PubMed: 26448331]

Lee H, Mortensen K, Sanggaard S, Koch P, Brunner H, Quistorff B, et al. Quantitative Gd-DOTA uptake from cerebrospinal fluid into rat brain using 3D VFA-SPGR at 9.4T. Magnetic resonance in medicine : official journal of the Society of Magnetic Resonance in Medicine /Society of Magnetic Resonance in Medicine 2018; 79(3): 1568–78.

Lee H, Xie L, Yu M, Kang H, Feng T, Deane R, et al. The Effect of Body Posture on Brain Glymphatic Transport. The Journal of neuroscience : the official journal of the Society for Neuroscience 2015; 35(31): 11034–44. [PubMed: 26245965]

Louveau A, Plog BA, Antila S, Alitalo K, Nedergaard M, Kipnis J. Understanding the functions and relationships of the glymphatic system and meningeal lymphatics. The Journal of clinical investigation 2017; 127(9): 3210–9. [PubMed: 28862640]

Mayeda ER, Whitmer RA, Yaffe K. Diabetes and cognition. Clinics in geriatric medicine 2015; 31(1): 101–15, ix. [PubMed: 25453304]

Mehla J, Chauhan BC, Chauhan NB. Experimental induction of type 2 diabetes in aging-accelerated mice triggered Alzheimer-like pathology and memory deficits. Journal of Alzheimer's disease : JAD 2014; 39(1): 145–62. [PubMed: 24121970]

Nejad-Davarani SP, Bagher-Ebadian H, Ewing JR, Noll DC, Mikkelsen T, Chopp M, et al. An extended vascular model for less biased estimation of permeability parameters in DCE-T1 images. NMR in biomedicine 2017a; 30(6).

Nejad-Davarani SP, Bagher-Ebadian H, Ewing JR, Noll DC, Mikkelsen T, Chopp M, et al. A parametric model of the brain vascular system for estimation of the arterial input function (AIF) at the tissue level. NMR in biomedicine 2017b; 30(5).

Nielsen S, Nagelhus EA, Amiry-Moghaddam M, Bourque C, Agre P, Ottersen OP. Specialized membrane domains for water transport in glial cells: high-resolution immunogold cytochemistry of aquaporin-4 in rat brain. The Journal of neuroscience : the official journal of the Society for Neuroscience 1997; 17(1): 171–80. [PubMed: 8987746]

Plog BA, Dashnaw ML, Hitomi E, Peng W, Liao Y, Lou N, et al. Biomarkers of traumatic injury are transported from brain to blood via the glymphatic system. The Journal of neuroscience : the official journal of the Society for Neuroscience 2015; 35(2): 518–26.

Prasad S, Sajja RK, Naik P, Cucullo L. Diabetes Mellitus and Blood-Brain Barrier Dysfunction: An Overview. Journal of pharmacovigilance 2014; 2(2): 125. [PubMed: 25632404]

Qiu C, Sigurdsson S, Zhang Q, Jonsdottir MK, Kjartansson O, Eiriksdottir G, et al. Diabetes, markers of brain pathology and cognitive function: the Age, Gene/Environment Susceptibility-Reykjavik Study. Ann Neurol 2014; 75(1): 138–46. [PubMed: 24243491]

Ramirez J, Berezuk C, McNeely AA, Gao F, McLaurin J, Black SE. Imaging the Perivascular Space as a Potential Biomarker of Neurovascular and Neurodegenerative Diseases. Cellular and molecular neurobiology 2016; 36(2): 289–99. [PubMed: 26993511]

Rangroo Thrane V, Thrane AS, Plog BA, Thiyagarajan M, Iliff JJ, Deane R, et al. Paravascular microcirculation facilitates rapid lipid transport and astrocyte signaling in the brain. Scientific reports 2013; 3: 2582. [PubMed: 24002448]

Ratner V, Gao Y, Lee H, Elkin R, Nedergaard M, Benveniste H, et al. Cerebrospinal and interstitial fluid transport via the glymphatic pathway modeled by optimal mass transport. NeuroImage 2017; 152: 530–7. [PubMed: 28323163]

Ratner V, Zhu L, Kolesov I, Nedergaard M, Benveniste H, Tannenbaum A. Optimal-mass-transfer-based estimation of glymphatic transport in living brain. Proceedings of SPIE--the International Society for Optical Engineering 2015; 9413.

Saczynski JS, Siggurdsson S, Jonsson PV, Eiriksdottir G, Olafsdottir E, Kjartansson O, et al. Glycemic status and brain injury in older individuals: the age gene/environment susceptibility-Reykjavik study. Diabetes care 2009; 32(9): 1608–13. [PubMed: 19509008]

Szeman B, Nagy G, Varga T, Veres-Szekely A, Sasvari M, Fitala D, et al. [Changes in cognitive function in patients with diabetes mellitus]. Orvosi hetilap 2012; 153(9): 323–9. [PubMed: 22348847]

Venkat P, Chopp M, Chen J. New insights into coupling and uncoupling of cerebral blood flow and metabolism in the brain. Croatian medical journal 2016; 57(3): 223–8. [PubMed: 27374823]

Wostyn P, Van Dam D, Audenaert K, Killer HE, De Deyn PP, De Groot V. A new glaucoma hypothesis: a role of glymphatic system dysfunction. Fluids and barriers of the CNS 2015; 12: 16. [PubMed: 26118970]

Wu O, Ostergaard L, Weisskoff RM, Benner T, Rosen BR, Sorensen AG. Tracer arrival timing-insensitive technique for estimating flow in MR perfusion-weighted imaging using singular value decomposition with a block-circulant deconvolution matrix. Magnetic resonance in medicine : official journal of the Society of Magnetic Resonance in Medicine / Society of Magnetic Resonance in Medicine 2003; 50(1): 164–74.

Wuerfel J, Haertle M, Waiczies H, Tysiak E, Bechmann I, Wernecke KD, et al. Perivascular spaces--MRI marker of inflammatory activity in the brain? Brain : a journal of neurology 2008; 131(Pt 9): 2332–40. [PubMed: 18676439]

Xie L, Kang H, Xu Q, Chen MJ, Liao Y, Thiyagarajan M, et al. Sleep drives metabolite clearance from the adult brain. Science 2013; 342(6156): 373–7. [PubMed: 24136970]

Yang HT, Sheen YJ, Kao CD, Chang CA, Hu YC, Lin JL. Association between the characteristics of metabolic syndrome and Alzheimer's disease. Metabolic brain disease 2013; 28(4): 597–604. [PubMed: 23644927]

Highlights

- Mathematical modeling of glymphatic system using local input function
- Map the glymphatic system pathways
- Derive kinetic parameters of the glymphatic system
- Provide quantitative maps of the structure and function of this system
- The developed maps are sensitive to diabetic induce brain changes

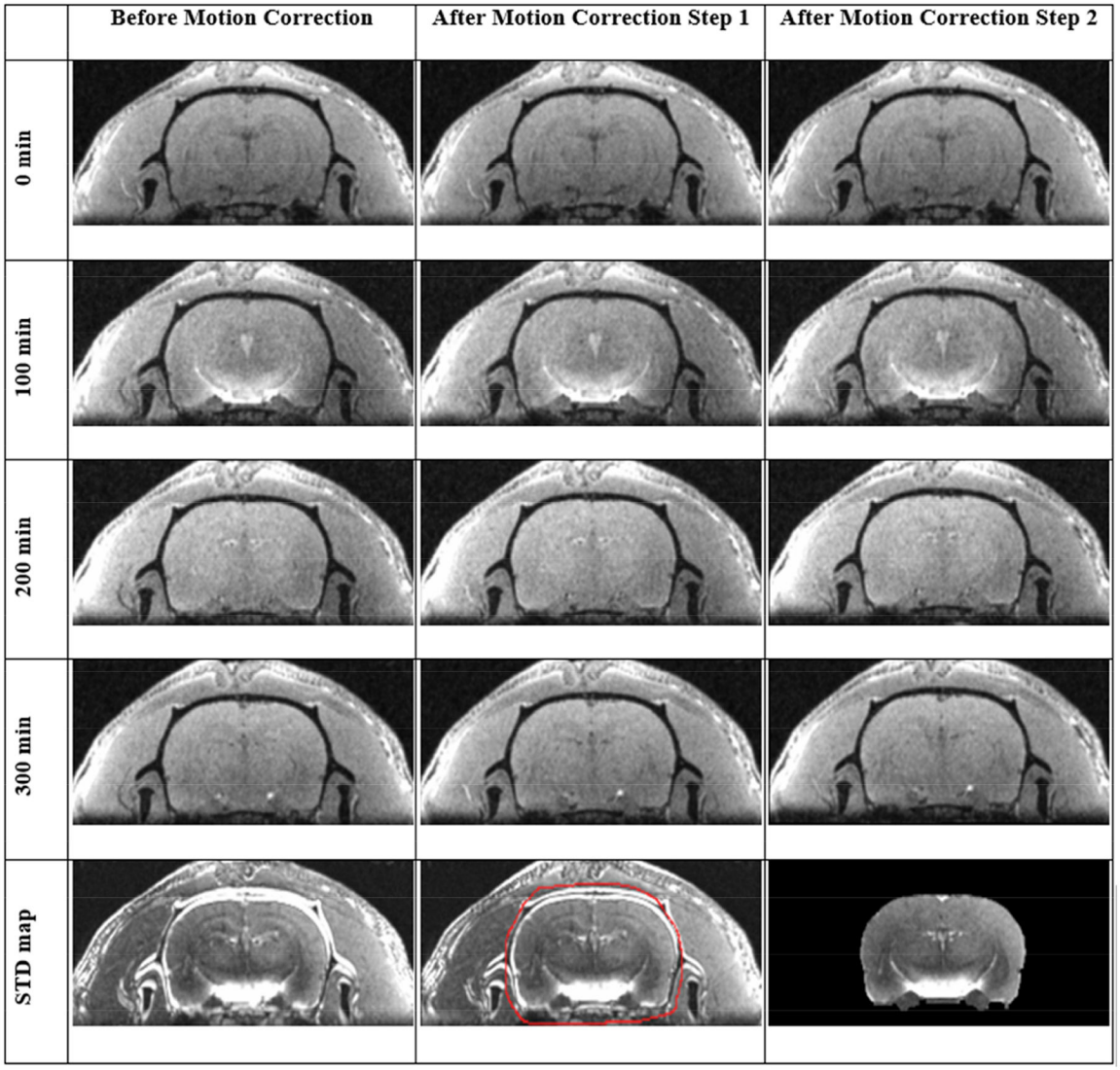

Figure 1. Illustration of motion correction steps for a typical case.

Four time points, 0, 100, 200, and 300 minutes after injection are displayed, representing the accumulation and dissipation of the tracer during the experiment. Although the motion cannot be seen clearly using these images, the corresponding STD maps can show the level of brain motion. As it can be seen from the STD maps, the edges have become clearer after the motion correction steps.

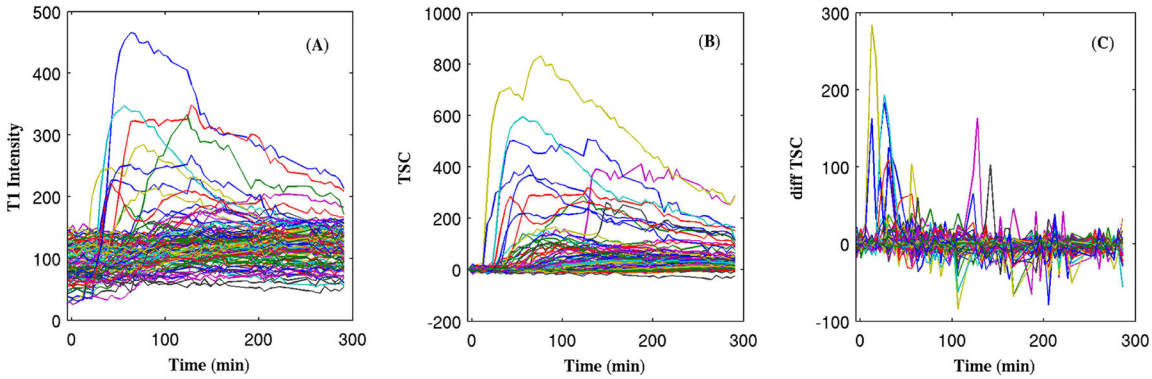

Figure 2. Illustration of signal change during the experiment of a typical case.

100 voxels were randomly selected and their intensity values on the T1-weighted images are plotted in (**A**). (**B**) The corresponding time signal curves (TSCs), calculated using equation (1). (**C**) The derivative signals of (**B**).

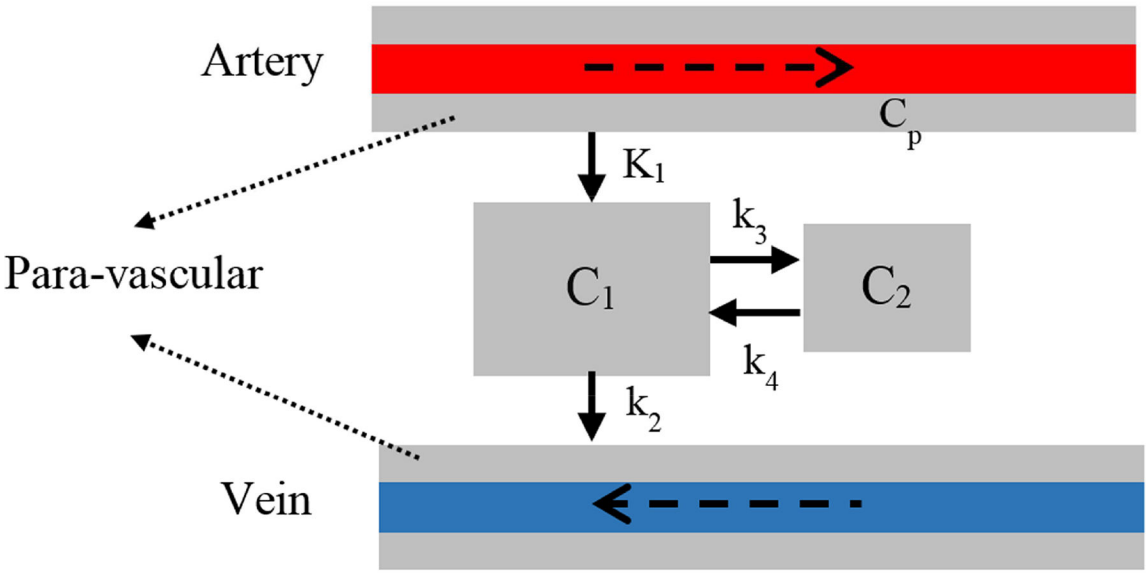

Figure 3.
Two compartment kinetic modeling of glymphatic paravascular CSF-ISF exchange.

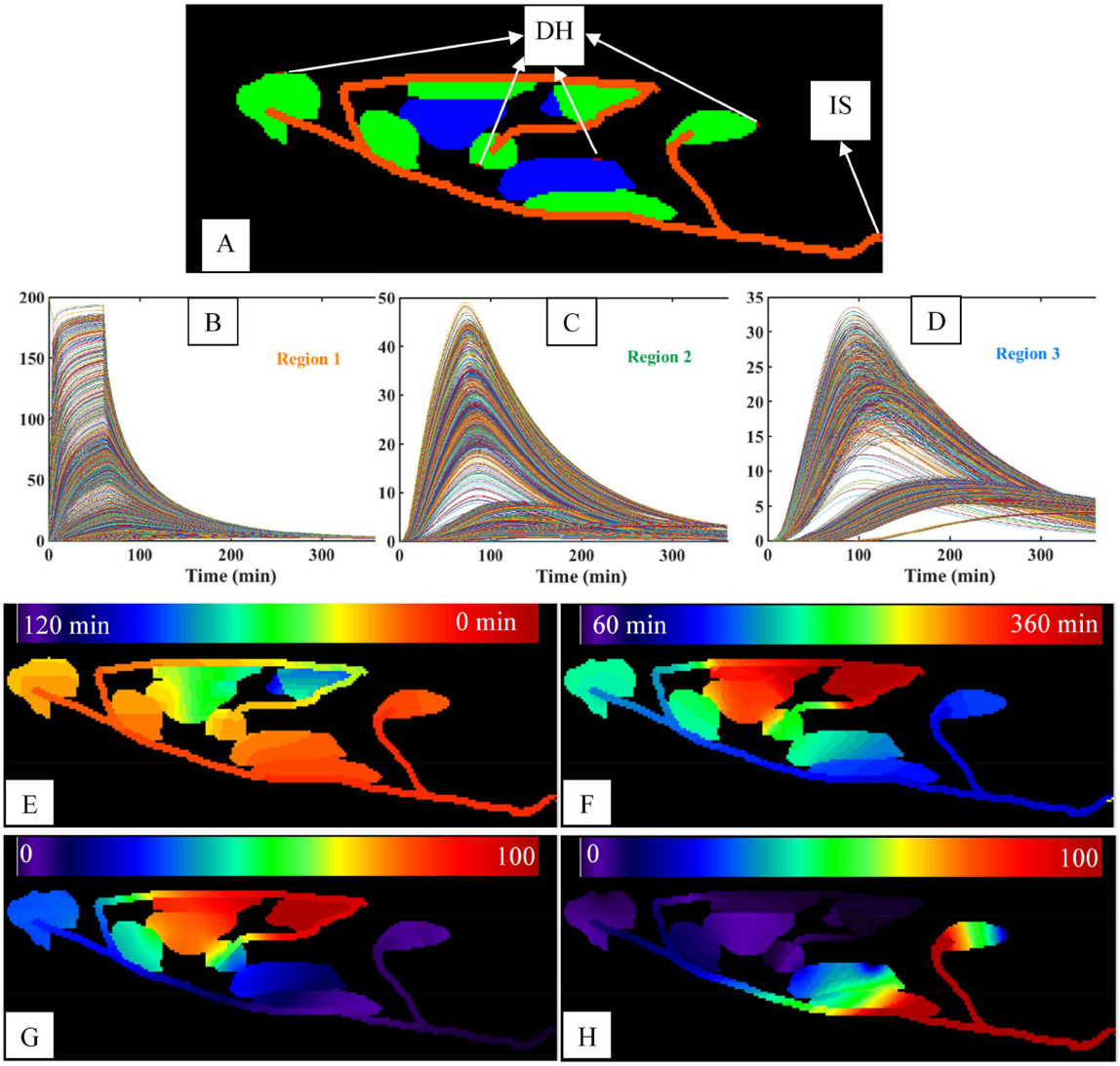

Figure 4. Generating artificial data.

(A) An imaginary path for contrast agent distribution consisting of three regions (region 1 : orange, region 2 : green, and region 3 : blue) and one infusion site (IS) and four drain holes (DM). The resulting temporal profiles for CA density in (B) region 1, (C) region 2, and (D) region 3. The resulting ground truth maps for the parameters (E) t_a, (F) t_{max}, (G) residual, and (H) infusion rate.

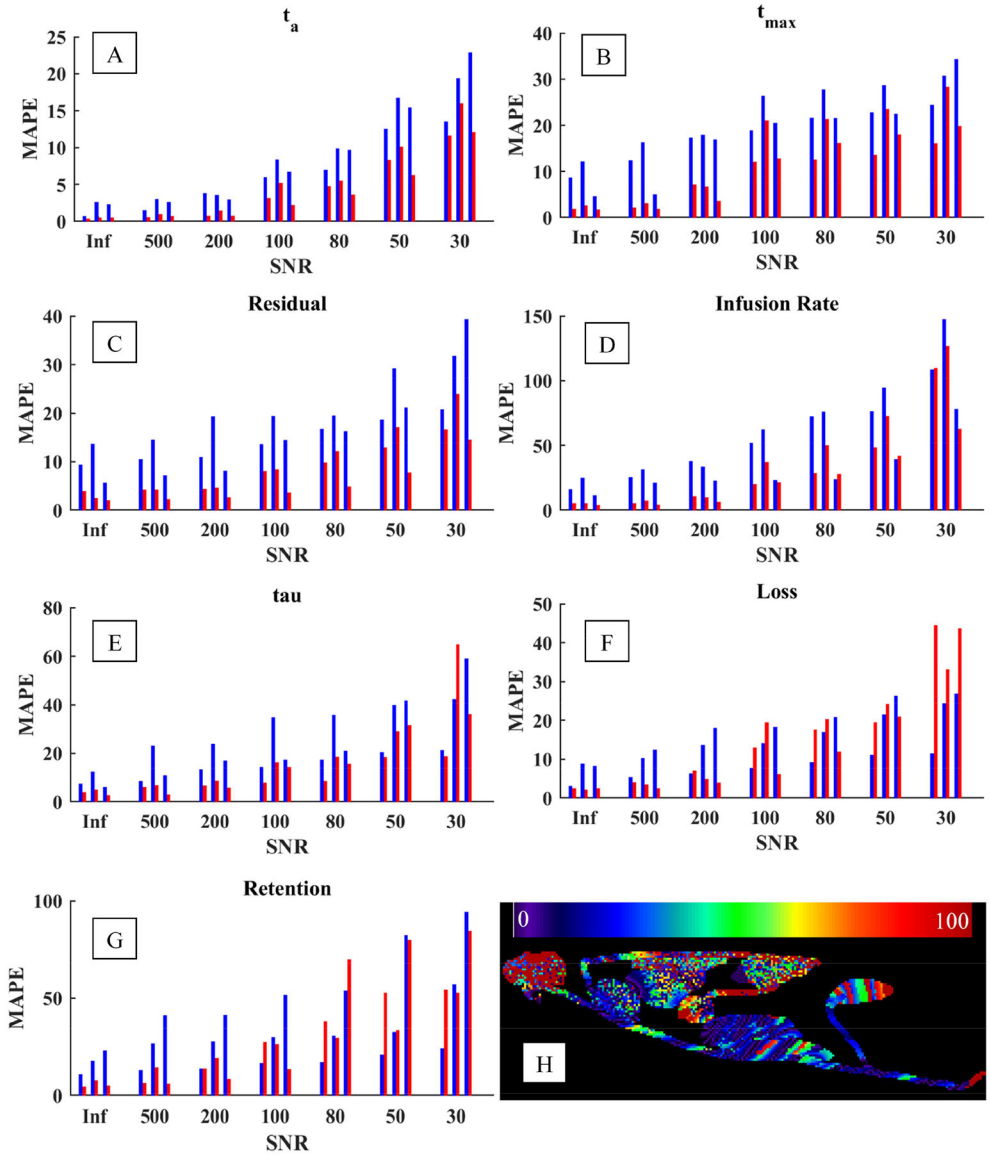

Figure 5. The mean absolute percentage error (MAPE) values for different parameters on different regions in different SNRs.

The blue and red bins correspond to the MAPEs from using the actual TSCs and the derivative of the TSCs for the clustering, respectively. For each SNR, the MAPE values are calculated on the three regions shown in Fig 4.A. (H) represents the MAPE map of residual parameter for the SNR of 80. Higher errors for the estimated parameters in the regions far from the infusion site is mainly due to the attenuation of the TSCs in these regions.

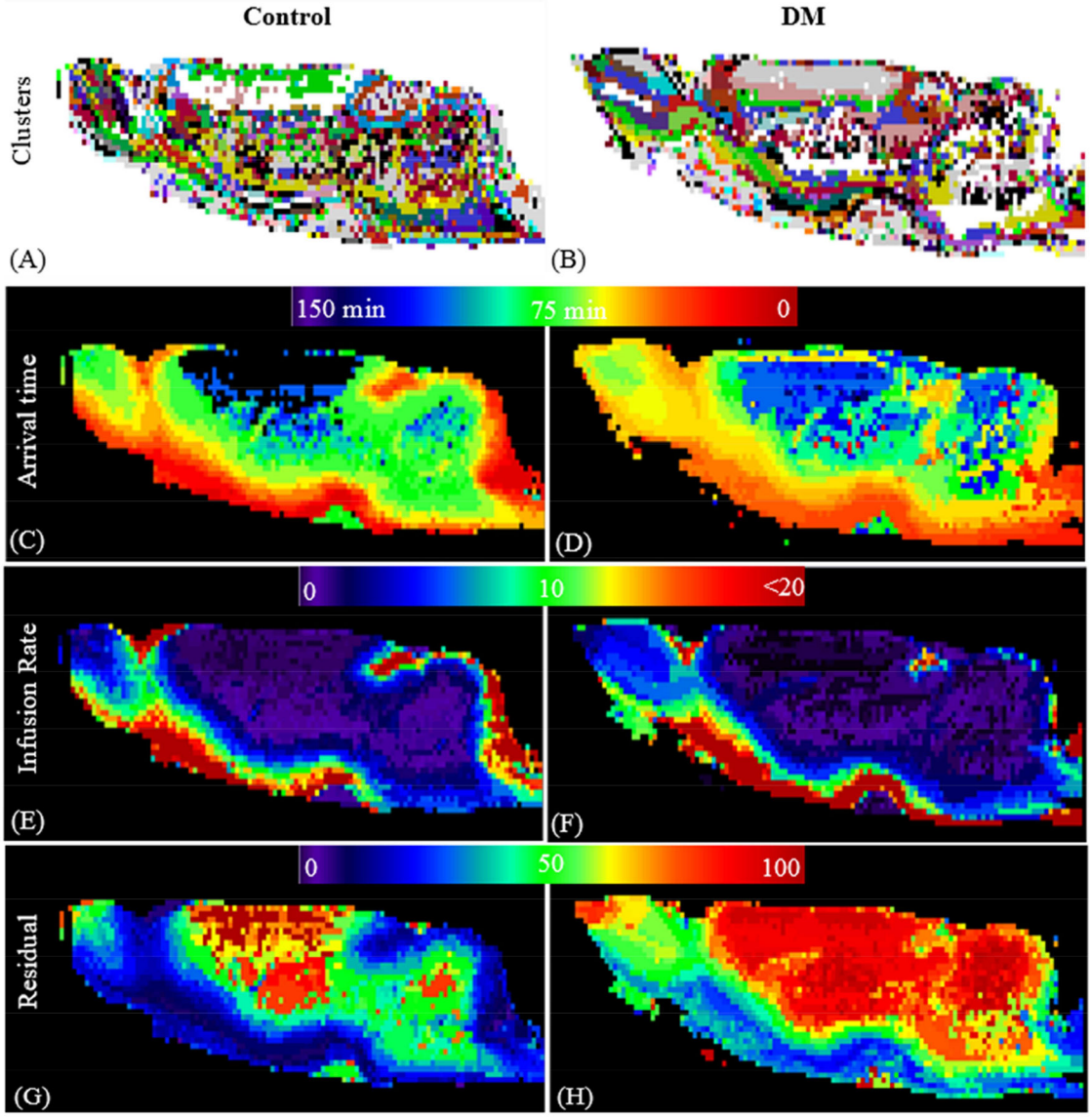

Figure 6. Resulting clustering maps and their corresponding scalar maps for one healthy control and one DM animal.

First row (**A** and **B**) shows the resulted clusters colored with random color-maps. Deep tissues are seen in big clusters because of weak infusion of the tracer to them. Second row (**C** and **D**) corresponds to arrival time (t_a) maps colored with cold and hot colors. The colder the color, the longer time the tracer arrives to the region. Lower bulk speed of CSF in the para-vasculatures of DM animal can be seen. Third row (**E** and **F**) shows the infusion rate maps with hot and cold color-maps. The hotter the color, the higher the infusion rate. These maps suggest higher infusion rate in the inferior para-vascular pathways of the DM animal. Forth row (**G** and **H**) corresponds to the contrast agent residual, *Res*. The hotter the color, the more amount of the CA remains at the end of experiment. Significant amount of Gd-DPTA has remained in the DM animal brain.

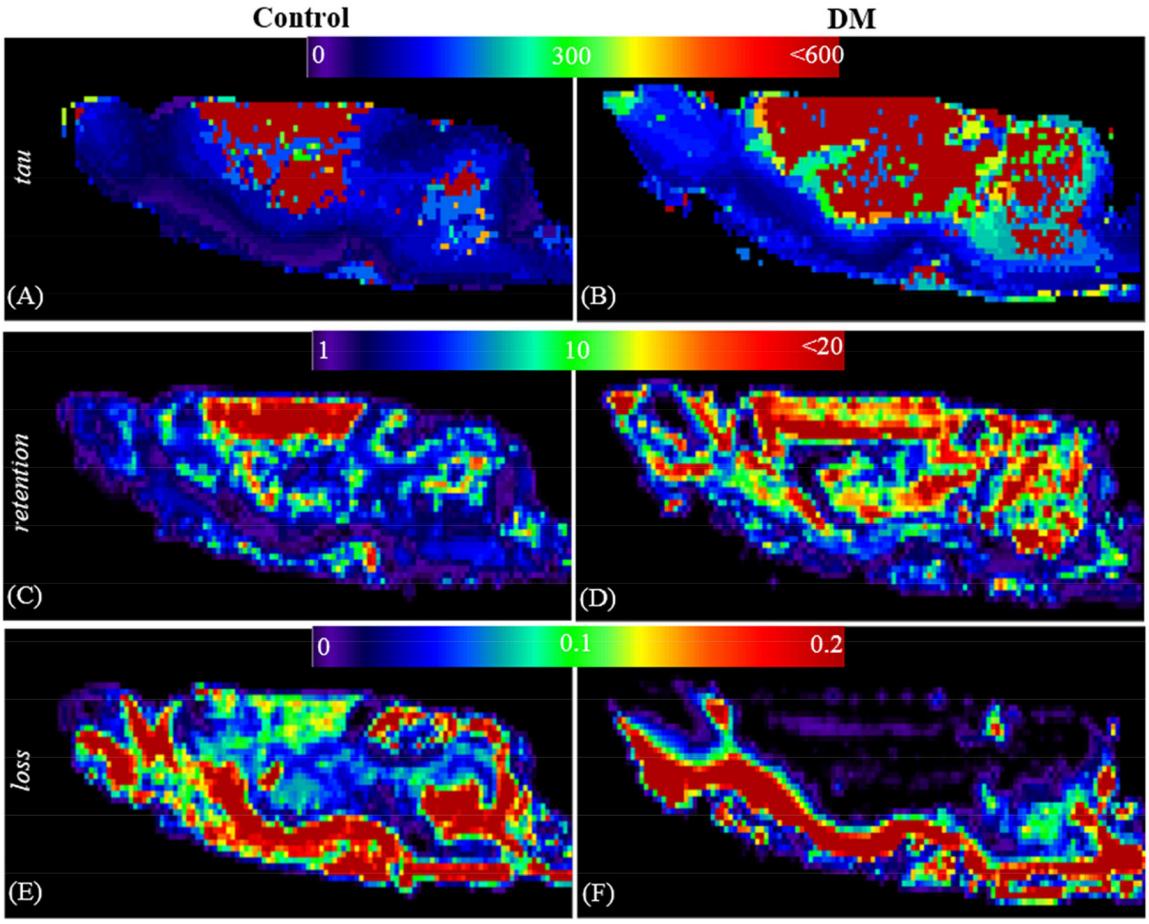

Figure 7. The resulting maps of quantitative modeling the glymphatic system for one healthy control and one DM animal.

First row (**A** and **B**) shows the clearance *time constant*, τ (minutes), resulted from one exponential model (equation 15). The longer time constant, the slower clearance of the CA from the tissue. The *retention* maps (equation 13) (**C** and **D**) and the *loss* maps (equation 14) (**E** and **F**) are estimated from the proposed two-compartment kinetic model shown in Fig. 3. The high retention values seen in the top central region of the control brain may be caused by low concentration of CA.

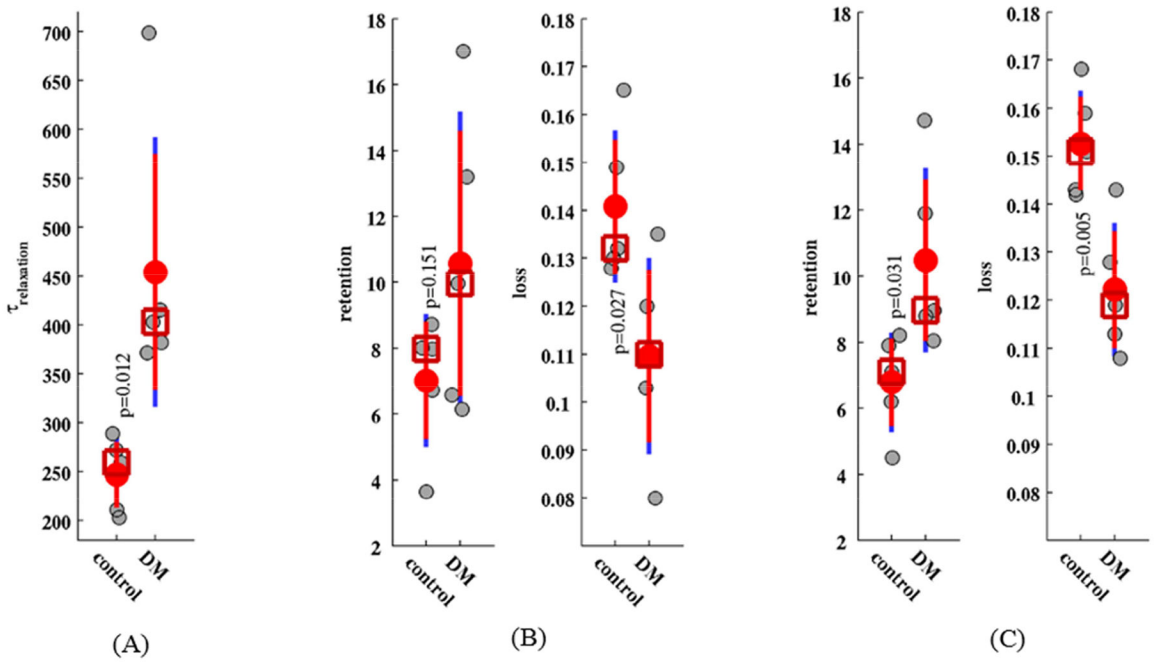

Figure 8. Boxplot representation of the estimated parameters.

(**A**) one-exponential, (**B**) two-compartment kinetic, and (**C**) proposed modified two-compartment kinetic models. The rectangles and circles show the median and mean values, respectively. For each parameter, a two sample t-test with the hypothesis that if the mean values of that parameter for the two groups are equal was performed and the resulted p-value is displayed on each plot. It can be seen that the estimated parameters from our proposed model discriminate the DM and control animals more significantly.